

A proximitized quantum dot in germanium

Lazar Lakic^{†,1}, William Iain L. Lawrie^{†,1}, David van Driel,² Lucas E. A. Stehouwer,² Menno Veldhorst,² Giordano Scappucci,² Ferdinand Kuemmeth,¹ and Anasua Chatterjee^{1,2,*}

¹*Center for Quantum Devices, Niels Bohr Institute,
University of Copenhagen, 2100 Copenhagen, Denmark*

²*QuTech and Kavli Institute of Nanoscience, Delft University of Technology, Delft, The Netherlands*
(Dated: May 10, 2024)

Planar germanium quantum wells have recently been shown to host a hard-gapped superconductor-semiconductor interface. Additionally, quantum dot spin qubits in germanium are well-suited for quantum information processing, with isotopic purification to a nuclear spin-free material expected to yield long coherence times. Therefore, as one of the few group IV materials with the potential to host superconductor-semiconductor hybrid devices, proximitized quantum dots in germanium are a crucial ingredient towards topological superconductivity and novel qubit modalities. Here we demonstrate a quantum dot (QD) in a Ge/SiGe heterostructure proximitized by a platinum germanosilicide (PtGeSi) superconducting lead (SC), forming a SC-QD-SC junction. We show tunability of the QD-SC coupling strength, as well as gate control of the ratio of charging energy and the induced gap. We further exploit this tunability by exhibiting control of the ground state of the system between even and odd parity. Furthermore, we characterize the critical magnetic field strengths, finding a robust critical out-of-plane field of 0.91 ± 0.05 T. Finally we explore sub-gap spin splitting in the device, observing rich physics in the resulting spectra, that we model using a zero-bandwidth model in the Yu-Shiba-Rusinov limit. The demonstration of controllable proximitization at the nanoscale of a germanium quantum dot opens up the physics of novel spin and superconducting qubits, and Josephson junction arrays in a group IV material.

INTRODUCTION

New and exotic physical phenomena can emerge in superconducting-semiconducting hybrids, enabling engineered quantum materials [2], circuit quantum electrodynamics (cQED) with novel superconducting qubits [3, 4], and topologically protected phases [5–8]. In particular, proximitized quantum dots constitute key building blocks for devices such as Cooper pair splitters, Kitaev chains [7, 8], and protected qubits [9, 10]. However, to date the majority of these experiments have been performed in group III-V materials where nuclear spins are unavoidable, critically hampering spin coherence, and where 2D heterostructures exhibit piezoelectricity, deleterious for cQED circuits. Conversely, silicon and germanium are established group IV material platforms to integrate spin qubits hosted in gate defined quantum dots [11, 12], with isotopic purification having proved a gamechanger for ultra-long spin qubit coherence [13]. Contrary to silicon [14], germanium forms low resistance Ohmic contacts due to intrinsic Fermi level pinning close to the valence band [15, 16]. This has motivated a strong effort to induce superconductivity [17–22] and very recently, hard-gap superconductivity has been demonstrated in mesoscopic devices implemented in a Ge/SiGe heterostructure [21, 22], in Ge/Si core shell nanowires [23] and in a cQED circuit [24].

Here, we present a superconducting-semiconducting hybrid quantum dot, which is hosted in Ge, a group IV material uniquely allowing for both isotopic purification [25] and a superconducting hard gap [21, 22]. Our demonstration in a two-dimensional heterostruc-

ture establishes a novel platform that exhibits enhanced scalability compared to nanowires, is compatible with radiofrequency-reflectometry readout [26] and a highly successful spin qubit platform [27–29]. It may therefore be useful for long-range qubit interactions mediated via crossed Andreev reflection [30, 31] as well as heterogeneous quantum processors [9, 32] incorporating spin [11, 12] and superconducting circuits [33]. Isotopically purified, proximitized germanium may be a crucial enabler for coherent Andreev spin qubits, protected superconducting qubits, and quantum dot-based Kitaev chains, and our first demonstration of a quantum dot with gate-tunable proximitization in a group IV heterostructure is a key ingredient.

In this work, superconducting polycrystalline Platinum-Germanium-silicide (PtSiGe) leads are formed by a controlled thermally-activated solid phase reaction between deposited platinum (Pt) and the heterostructure (Ge/SiGe) [21]. Importantly, the PtGeSi leads alleviate the need to etch into the heterostructure to deposit or pattern the superconductor, a potential source of damage exposing the quantum well and interface to air and processing. The leads act as charge reservoirs and as proximitization for the quantum dot (QD). We first demonstrate Coulomb blockade physics of a QD coupled to two superconducting leads (SC) forming a SC-QD-SC junction. We identify a superconducting gap energy window of 4Δ inside which transport is suppressed, and outside which standard Coulomb diamonds are recovered. We observe sub-gap states in transport upon increasing the QD-SC coupling Γ_S , which is consistent with the formation of Yu-Shiba-Rusinov (YSR) states in

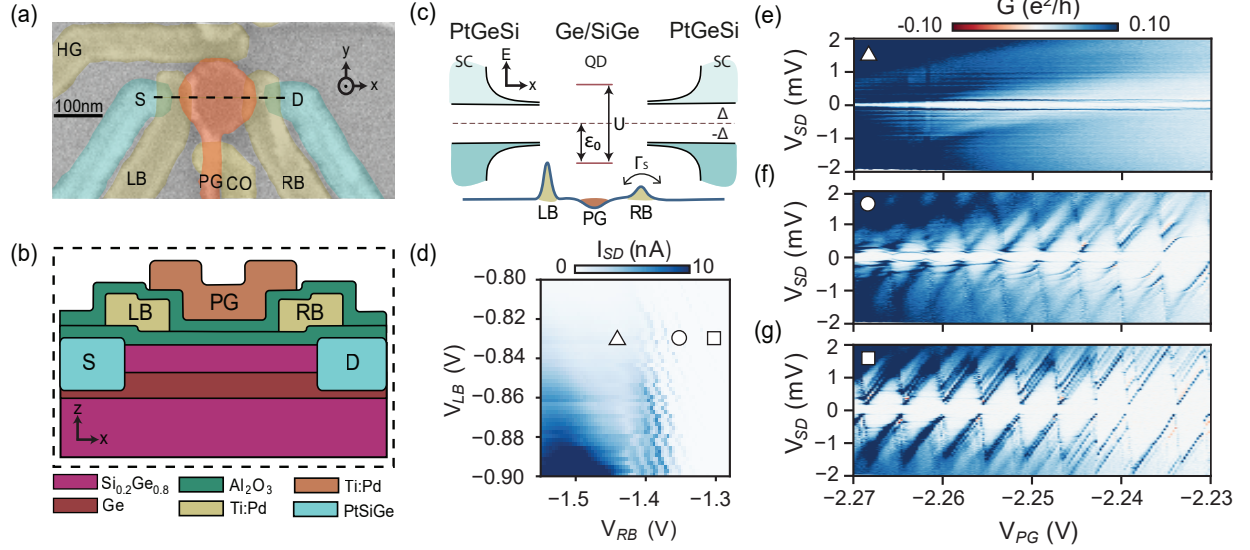


FIG. 1. (a) False coloured scanning electron micrograph (SEM) of a nominally identical device. The device comprises three lithographically defined metallic layers, separated by a dielectric of Al_2O_3 grown using atomic layer deposition (ALD). A plunger gate PG (orange) controls the electrochemical potential of the quantum dot. The coupling of the quantum dot to the superconducting PtSiGe leads S and D is controlled by two barrier gates LB and RB (yellow). A cut-off gate CO prevents accumulation beneath the gate fan-out of PG, and a helper gate HG provides further control of the quantum dot confinement. (b) Heterostructure and gate stack schematic corresponding to the cross section indicated by the black dashed line in (a). (c) Energy schematic depicting the physical system in (a). Here, Δ is the SC gap energy, U the charging energy of the QD, Γ_S the hybridization energy of the SC and QD and ϵ_0 the electrochemical potential of the QD with respect to the SC Fermi energy. (d) Source-drain current I_{SD} as a function of barrier gates V_{LB} and V_{RB} at bias voltage $V_{SD} = 500 \mu\text{V}$. The square, circle and triangle correspond to the indicated gate voltage setting in (e), (f) and (g). (e-g) Bias spectroscopy for the three gate voltages indicated in (d), with high, moderate and low coupling of the quantum dot to the superconducting leads respectively, showing a transition between strongly coupled lead (e) and weakly coupled lead (g). Negative differential conductance observed may indicate Coulomb diamonds of odd occupancy. [1].

the system [34, 35]. We demonstrate gate control of Γ_S by tuning the ground state at half-filling from a singlet state to a doublet state [36]. We then study the critical magnetic field of the hybrid device, finding a robust out-of-plane critical magnetic field $B_{\perp}^c = 0.91 \pm 0.05 \text{ T}$. Finally, we investigate spin-splitting in the SC-QD-SC system, finding a g -factor of 1.5 ± 0.2 for an out-of-plane magnetic field, and also characterize the g -tensor anisotropy. To explain the energy splitting observed in the SC-QD-SC system we use a zero bandwidth (ZBW) Anderson Impurity model [37, 38] with the possibility of Zeeman splitting on the SC. Our observation of controllable subgap states and subgap spin splitting, magnetic field resilience, and the high tunability of the quantum dot-superconducting coupling establishes Ge/SiGe and PtSiGe as an attractive platform for hybrid quantum information processing.

RESULTS

We utilize established fabrication protocols for quantum dot fabrication [40] and superconducting contacts [21] in Ge/SiGe quantum wells [41], to create

a quantum dot coupled to two superconducting leads formed by rapid thermal annealing of Pt at 400°C in Ar atmosphere for 15 minutes. Figure 1a shows a false-colored scanning electron micrograph of the device, consisting of one lithographically-defined layer for the superconducting leads (cyan) and two layers of electrostatic gates (yellow and orange, see Methods section for further details). Figure 1b shows a schematic of the cross-section of the device heterostructure and gate stack. Layers are electrically isolated from one another by 7 nm of Al_2O_3 deposited by atomic layer deposition at 150°C . Barrier gates (LB, RB) control Γ_S , while the plunger gate (PG) controls the relative electrochemical potential of the quantum dot levels with respect to the superconducting leads (ϵ_0) as seen in Figure 1c. Two gates (HG and CO) are also used to confine the quantum dot and prevent unwanted accumulation. We utilize standard DC transport and low frequency lock-in techniques to measure source-drain current I_{SD} and differential conductance G across the quantum dot. Notably, our device is also connected to a radiofrequency (RF) reflectometry circuit via the source superconducting lead, and additional datasets in the low-coupling regime measured using this RF probe are

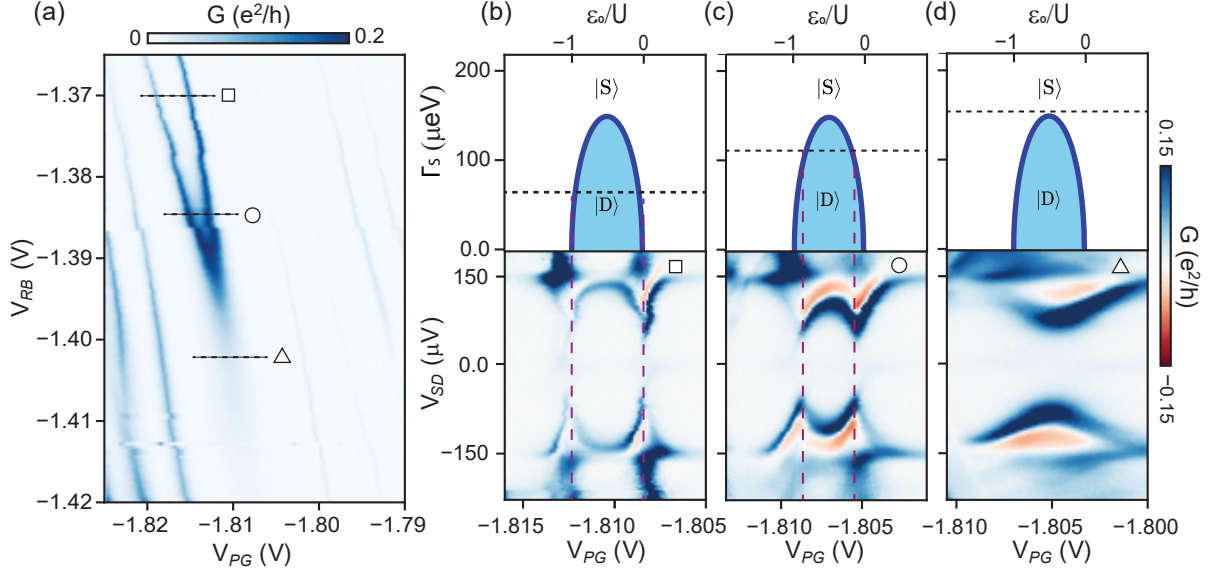


FIG. 2. **(a)** Charge stability diagram of V_{RB} vs V_{PG} at $V_{SD} = 80 \mu\text{V}$. **(b-d)** Bottom panels show bias spectroscopy at decreasing values of V_{RB} corresponding to the square, circle, and triangle icons in panel a. Upper panels portray qualitative phase diagrams following ref. [39] of the expected ground state character of the hybrid system. Here, ϵ_0 is the electrochemical potential of the quantum dot with respect to the grounded superconducting leads, and U is the charging energy of the quantum dot. As the SC-QD coupling Γ_S is increased, the doublet state becomes energetically unfavorable, as seen by the merging of charge transitions (purple dashed lines). Γ_S is roughly estimated by modelling the sub-gap spectrum in the bottom panels (see Supplementary Information), to be $70 \mu\text{eV}$, $110 \mu\text{eV}$, and $150 \mu\text{eV}$ from b-d respectively, as indicated by the black dashed lines.

presented in the Supplementary Information.

All data are taken at a lock-in frequency of 119 Hz , and amplitude of $2.5 \mu\text{V}$. Figure 1d shows I_{SD} as a function of the tunnel barrier V_{LB} and V_{RB} . Here, the source drain bias energy is set to $eV_{SD} = 300 \mu\text{eV}$ such that it exceeds the expected zero-field superconducting gap energy of $\sim 70 \mu\text{eV}$ [21]. We set V_{LB} close to its pinch-off value such that it acts as a tunnel probe, and vary V_{RB} to tune the coupling between superconductor and quantum dot Γ_S (Figure 1c). Figures 1e-g show bias spectroscopy at different values of V_{RB} . In the strong coupling regime (Figure 1e), we observe a range in bias energy of $4\Delta_0$ where transport is suppressed, from which we extract a superconducting pairing amplitude of $\Delta_0 = 72 \pm 6 \mu\text{eV}$, in its fully open state. Figure 1f shows that as Γ_S is decreased (positive change on V_{RB}), we observe tunnel-broadened Coulomb oscillations and sub-gap transport features, indicating a hybridized QD. At low coupling between the QD and SC (Fig. 1g) we observe sharp Coulomb diamonds outside a bias window of $\pm 2\Delta_0$. We conclude that we have versatile electrostatic control of the degree of hybridization of a quantum dot with a superconductor, consistent with experiments performed in InAs-Al nanowires [42] and InSbAs-Al 2DEGs [7].

Singlet-doublet quantum phase transition

A quantum dot coupled to a superconducting lead at half-occupancy of charges can have two different ground states, depending on the degree of superconductor-quantum dot coupling. At low coupling strengths and zero magnetic field strength, the ground state at half-filling, ie. $\epsilon_0/U = 0.5$, will be a spin-degenerate doublet state $|D\rangle = \{|\downarrow\rangle, |\uparrow\rangle\}$. Here, ϵ_0 is the electrochemical potential of the QD with respect to the SC lead and U is the charging energy of the QD. At high coupling, a preference for superconducting pairing will dominate, leading to a singlet ground state $|S\rangle = u|0\rangle - v|2\rangle$. By utilizing the control of Γ_S demonstrated above, we show that we can tune between these ground states. We operate in a regime whereby V_{LB} is very close to its pinch-off value, such that it acts as a tunneling probe. We then vary V_{RB} to tune the coupling Γ_S . Figure 2a shows a charge stability diagram of the system with the QD plunger gate V_{PG} on the horizontal axis, and the QD-SC barrier gate V_{RB} on the vertical axis, at a bias energy of $eV_{SD} = 80 \mu\text{eV}$, slightly above Δ . The vertical lines measured are Coulomb resonances indicating transitions between the N , $N+1$ and $N+2$ occupations of the quantum dot (from right to left). As we increase Γ_S by making RB more negative we observe the merging of two levels at $V_{RB} = -1.395 \text{ V}$.

We further investigate these transitions with bias spectroscopy as a function of plunger gate voltage at different

values of V_{RB} . In the bottom panel of Figure 2b, we show bias spectroscopy at $V_{RB} = -1.37$ V (square in Figure 2a) for varying V_{SD} and V_{PG} . At V_{PG} values of -1.81 V and -1.808 V, the state crosses Δ_0 , signalling the changes in ground state parity as seen from 2a.

In the bottom panel of Figure 2c, we show spectroscopy at $V_{RB} = -1.385$ V (circle in Figure 2a). We see an evolution of the state features into a characteristic eye-shape indicating the formation of YSR states [34, 43–46] on the hybridized QD. The negative differential conductance is attributed to probing sub-gap features with a coherence peak [47]. In the bottom panel of Figure 2d, we perform bias spectroscopy at $V_{RB} = -1.4025$ V (triangle in Figure 2a) showing no parity change, which we interpret as the QD filling remaining in a singlet ground state upon loading an additional hole.

In QD-SC systems, where the charging energy of the QD U is larger than the SC order parameter Δ , quasiparticles in the SC can bind to the dot by the exchange interaction and give rise to sub-gap excitations in the form of YSR states. Such systems can be modelled using a zero-bandwidth (ZBW) model that describes a quantum dot coupled to a single superconducting orbital [37, 48], which predicts which ground state the system prefers depending on the degree of hybridization between the SC and the QD. By solving the ZBW for where the energy of the singlet equals the one of the doublet, a singlet doublet phase transition diagram can be realized. In the top panels of Figure 2b-d such a phase transition has been illustrated and dashed lines have been inserted at Γ_S values based on extracted coupling values (70 μ eV, 110 μ eV, and 150 μ eV from b-d respectively), using the aforementioned minimal ZBW model (see Supplementary Information). As the hybridization energy Γ_S increases, it becomes less favorable to maintain the $|D\rangle$ ground state. The vertical dashed lines indicate a qualitative correspondence between the experimental barrier gate RB controlling Γ_S , and the calculated Γ_S in the phase diagram. The magenta stippled lines in the bottom panels serve as guides to the eye to indicate where the phase transition occurs.

Magnetic field characterization

We now turn to the magnetic field dependence of the superconducting parent gap. Figure 3a shows bias spectroscopy of the quantum dot in the few hole and low Γ_S regime, as a function of out-of-plane magnetic field strength B_\perp . We fit the closing of the superconducting gap according to $\Delta(B) = 2\Delta_0\sqrt{1 - (B/B_c)^2}$ [49], where Δ_0 is the superconducting gap at zero magnetic field, and B_c is the critical magnetic field. We extract a critical field of $B_{c,\perp} = 0.91 \pm 0.05$ T. This greatly exceeds the critical field measured in prior studies, where the critical out-of-plane magnetic field was measured to

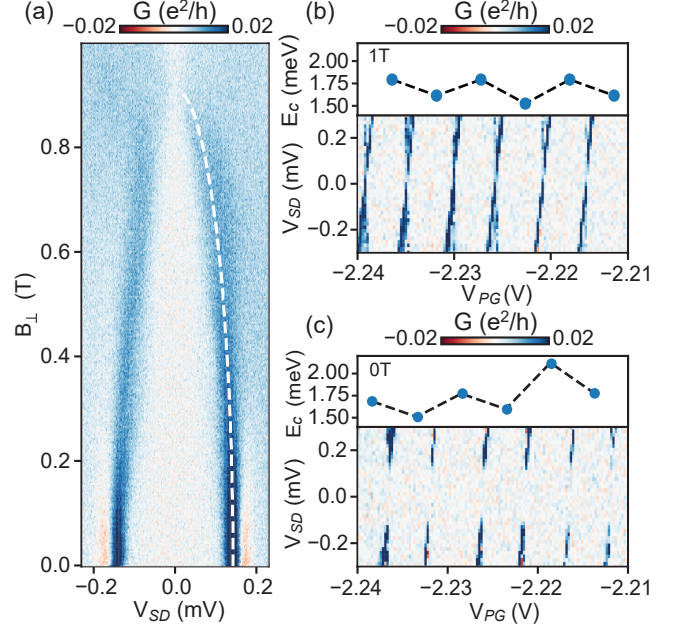


FIG. 3. **(a)** Bias spectroscopy as a function of out-of-plane magnetic field B_\perp . We extract a critical field $B_{c,\perp} = 0.91 \pm 0.05$ T. **(b-c)** Bias spectroscopy at low Γ_S , for out-of-plane magnetic field $B_\perp = 1$ T, and $B_\perp = 0$ T respectively. Top panels show extracted charging energies from Coulomb diamonds below.

be approximately 50 mT [21]. This disparity could be due to the smaller size of the superconducting junctions and leads [50] measured in the present experiment compared to those in ref. [21], which may alleviate vortex formation. We also characterize the critical magnetic field strengths for the two in-plane axes in Supplementary Section II. Figures 3b and 3c show bias spectroscopy of the quantum dot in the low coupling limit, taken at 1 T and 0 T respectively. At 0 T the superconducting gap is present within the Coulomb diamonds (Figure 3b), while normal Coulomb diamonds are recovered at 1 T due to the breaking down of superconductivity (Figure 3c). In both cases we find an even-odd oscillation in the filling structure at both low and high field strengths as seen in the top panels of Figures 3b and 3c, depicting the addition energy of each Coulomb diamond below, consistent with that observed previously in germanium [51] and InAs [43] QDs. The charging energy of the quantum dot varies between even and odd periodicity, indicating that the quantum dot is in the low hole occupancy. The charging energy is typically between 1 and 1.8 meV, more than ten times the superconducting gap, supporting our interpretation that we are in the YSR regime.

Finally we study the transport spectrum under the influence of a magnetic field in the same electrostatic regime as Figure 2b-c. Figures 4a-c show bias spec-

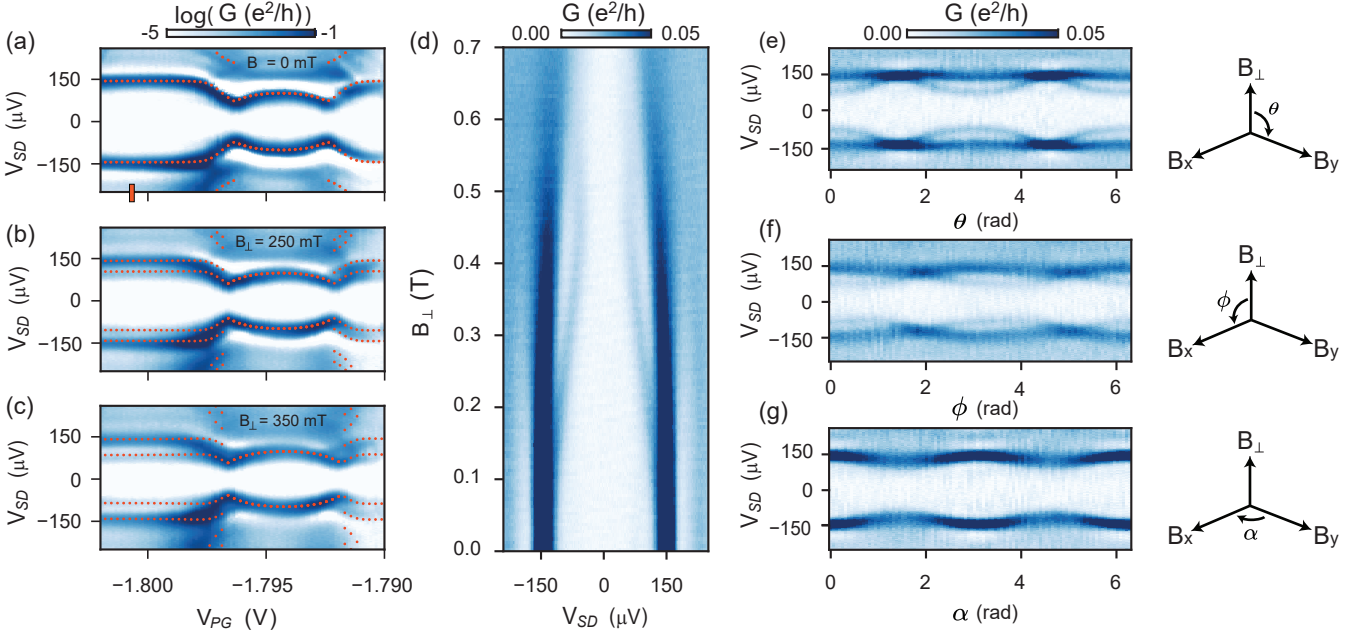


FIG. 4. **(a-c)** Bias spectroscopy displayed in logarithmic scale at magnetic field strengths of 0 mT, 250 mT and 350 mT respectively. Sub-gap energy splitting is visible in b) and c). The superimposed orange markers in Figures a-c serve as a qualitative comparison between the measured transport data and calculations using a zero-bandwidth model, inputting a $\Delta_0 = 72 \mu\text{eV}$, hybridization energy $\Gamma_S = 110 \mu\text{eV}$, charging energy $U = 1.6 \text{ meV}$, as well as a Zeeman energy of $E_z^{SC} = 0 \mu\text{eV}$ on the SC and $E_z^{QD} = 0 \mu\text{eV}$ on the QD, $E_z^{SC} = 44 \mu\text{eV}$ on the SC and $E_z^{QD} = 44 \mu\text{eV}$ on the QD, and $E_z^{SC} = 56 \mu\text{eV}$ on the SC and $E_z^{QD} = 56 \mu\text{eV}$ on the QD, respectively. **(d)** Magnetic field sweep at $V_{PG} = -1.8015 \text{ V}$. We extract a g-factor for the out-of-plane magnetic field splitting $g_{\perp} = 1.5 \pm 0.2$. **(e-g)** Bias spectroscopy of rotating magnetic field at total magnetic field strength $|B| = 400 \text{ mT}$ and $V_{PG} = -1.8017 \text{ V}$. Strong g -tensor anisotropy is observed between out-of-plane and in-plane magnetic field orientations.

troscopy measurements as a function of V_{PG} portrayed in logarithmic scale for enhanced visibility, taken at a perpendicular magnetic field, at strengths of (a) 0 mT, (b) 250 mT, and (c) 350 mT (see Supplementary Information for data in non-logarithmic scale). At 0 mT a $|S\rangle\text{-}|D\rangle\text{-}|S\rangle$ transition spectrum is observed, as seen in Figure 2b-c. A qualitative ZBW model of the system is plotted on top of the data as described previously (see Supplementary Information for details of the model), using a SC pairing energy of $\Delta_0 = 72 \mu\text{eV}$, a hybridization energy of $\Gamma_S = 110 \mu\text{eV}$, and a QD charging energy of $U = 1.6 \text{ meV}$. As we increase the perpendicular field an energy splitting of the subgap states is observed in the singlet ground-state sectors 4b-c. Interestingly, the energy splitting seen in the even parity groundstates have a flat energy dispersion indicating either a spin splitting of the parent gap itself, or of a strongly coupled sub-gap state, which we attribute to spinful excited quasiparticles. To qualitatively model the data, we introduce a Zeeman splitting term into the ZBW model for both the SC and QD. We find that setting the g-factor of the QD and superconducting orbitals to be equal in magnitude is sufficient to phenomenologically model the data potentially due to a g-factor renormalization as a result of hybridization [52, 53]. Additional data at lower mag-

netic field strength and lower coupling, supporting our hypothesis of g-factor renormalization, is reported in the Supplementary Information, as well as results from our ZBW model with varying system parameters.

In Figure 4d, we set the plunger gate voltage V_{PG} to -1.8017 V (orange notch in Figure 4a) and perform bias spectroscopy as a function of B_{\perp} from 0 T to 0.7 T. We observe the magnetic field splitting of the superconducting coherence peaks, and extract an out-of-plane g-factor, $g_{\perp} = 1.5 \pm 0.2$. This value is several times larger than the g-factor measured for magnetic fields close to in-plane in planar germanium quantum wells [54, 55], and several times smaller than the value reported in ref. [56] for out of plane g-factors. Furthermore, in a regime of lower coupling for the YSR states, we have measured an out-of-plane g-factor of $g_{\perp} = 4.5 \pm 0.6$ (see Supplementary Information, Figure S1) and a $g_{\perp} = 5.3 \pm 0.8$ in out-of-gap Coulomb diamond spectroscopy (see Supplementary Information, Figure S2). These observations support the hypothesis that the g-factor g_{\perp} either describes the quasiparticle coherence peaks, or is due to renormalization of the Ge/SiGe hole g -factor as a result of hybridization with the superconductor [52, 53].

Finally, we investigate anisotropy of the g-factor by performing bias spectroscopy as a function of magnetic field orientation. Figures 4e-g show bias spectroscopy at a magnetic field strength of $|B| = 400$ mT. The splitting is then investigated as a function of rotation angles. Here, the rotation angles θ , ϕ and α are defined as shown in Figure 4e-g. A large anisotropy is measured; while g-tensor anisotropy is ubiquitous for heavy holes in strained planar Ge/SiGe wells, it is seldom observed for a superconducting gap edge. On the other hand, anisotropic g-tensors have been observed in heavy fermion bulk superconductors, which could additionally explain the non-dispersive splitting in Fig. 4b-c [57]. We stress that our use of the annealed poly-crystalline superconductor Pt-GeSi is a recent material development in itself, and the physics of superconductivity in these nanoscale thin films is not fully understood. However, this anisotropy could also be explained by a sub-gap state in the QD that is strongly coupled to the superconductor.

CONCLUSION

We have demonstrated a quantum dot in Ge/SiGe proximitized by a superconducting lead and exhibiting robust YSR states. We find that the coupling between quantum dot and superconducting lead is highly tunable, as evidenced by the tunnel barrier controllability of the singlet or doublet nature of the YSR ground state at half-filling. Additionally, we have characterized the critical magnetic field strength, finding a robust out-of-plane critical field of ~ 0.91 T. Finally, we observe Zeeman splitting of sub-gap states, which we explain using a modified zero-bandwidth Anderson impurity model. The ability to tunably and strongly couple a superconductor to a quantum dot, in combination with a robust critical magnetic field, demonstrates the feasibility of our platform for hybrid germanium quantum information processing, including Andreev spin qubits and topological quantum computing, as well as the exploration of fundamental physics with superconductor-semiconductor devices. While the in-plane g-tensor component of holes in germanium planar wells is lower than in established group III-V platforms, it could be enhanced by confinement-induced g-factor engineering [58], and the out-of-plane g-factor could provide an alternative route to engineering topologically protected qubits using QD-SC chains [59]. Further work on RF-reflectometry-based measurements (as described in the Supplementary Information) could help achieve charge sensing and parity readout. Our demonstration in a group IV material, amenable to isotopic purification, constitutes a crucial building block for superconducting-semiconducting hybrid technologies and opens up previously inaccessible experimental directions.

[†] These authors contributed equally.

AUTHOR INFORMATION

L.E.A.S and G.S. grew and supplied the Ge/SiGe heterostructures and developed processes for the PtGeSi contacts. L.L. and W.I.L.L. designed the devices. L.L. fabricated the devices. L.L. and W.I.L.L. performed the experiment in the dilution refrigerator along with D.v.D., and analysed the data. L.L. performed numerical simulations within the ZBW model with help from D.v.D. and W.I.L.L. L.L. and W.I.L.L. wrote the manuscript with input from D.v.D., M.V., G.S., F.K. and A.C. A.C. and F.K. supervised the project.

ACKNOWLEDGMENTS

We thank J. Paaske, V. Baran and G. Mazur for valuable discussions. This project has received funding from the European Research Council (ERC) as part of the project NONLOCAL under grant agreement No 856526, and through the IGNITE project under grant agreement No. 101069515 of the Horizon Europe Framework Programme. AC acknowledges support from the Inge Lehmann Programme of the Independent Research Fund Denmark. We acknowledge funding by the Casimir PhD Travel Grant.

DATA AVAILABILITY

Raw data and analysis scripts for all data included in this work are available at the Zenodo data repository at <https://doi.org/10.5281/zenodo.11088753>.

* anasua.chatterjee@tudelft.nl

- [1] S. De Franceschi, L. Kouwenhoven, C. Schoenenberger, and W. Wernsdorfer, Hybrid superconductor–quantum dot devices, *Nature Nanotechnology* **5**, 703 (2010).
- [2] C. Böttcher, F. Nichele, and M. e. a. Kjaergaard, Superconducting, insulating and anomalous metallic regimes in a gated two-dimensional semiconductor–superconductor array, *Nature Physics*, 1138–1144 (2018).
- [3] M. Hays, V. Fatemi, D. Bouman, J. Cerrillo, S. Diamond, K. Serniak, T. Connolly, P. Krogstrup, J. Nygård, A. L. Yeyati, A. Geresdi, and M. H. Devoret, Coherent manipulation of an andreev spin qubit, *Science* **373**, 430 (2021).
- [4] A. Bargerbos, M. Pita-Vidal, R. Zitko, L. J. Splitthoff, L. Grunhaupt, J. J. Wesdorp, Y. Liu, L. P. Kouwenhoven, R. Aguado, C. K. Andersen, A. Kou, and B. van Heck, Spectroscopy of spin-split andreev levels in a quantum

- dot with superconducting leads, *Phys. Rev. Lett.* **131**, 097001 (2023).
- [5] M. Leijnse and K. Flensberg, Parity qubits and poor man's majorana bound states in double quantum dots, *Phys. Rev. B* **86**, 134528 (2012).
 - [6] A. Y. Kitaev, Unpaired majorana fermions in quantum wires, *Physics-Uspekhi* **44**, 10.1070/1063-7869/44/10S/S29 (2001).
 - [7] S. L. ten Haaf, Q. Wang, A. M. Bozkurt, C.-X. Liu, I. Kulesh, P. Kim, D. Xiao, C. Thomas, M. J. Manfra, T. Dvir, *et al.*, Engineering majorana bound states in coupled quantum dots in a two-dimensional electron gas, arXiv preprint [arXiv:2311.03208](https://arxiv.org/abs/2311.03208) (2023).
 - [8] T. Dvir, G. Wang, N. van Loo, C.-X. Liu, G. P. Mazur, A. Bordin, S. L. Ten Haaf, J.-Y. Wang, D. van Driel, F. Zatelli, *et al.*, Realization of a minimal kitaev chain in coupled quantum dots, *Nature* **614**, 445 (2023).
 - [9] D. M. Pino, R. S. Souto, and R. Aguado, Minimal kitaev-transmon qubit based on double quantum dots, *Phys. Rev. B* **109**, 075101 (2024).
 - [10] Q. Wang, S. L. D. ten Haaf, I. Kulesh, D. Xiao, C. Thomas, M. J. Manfra, and S. Goswami, Triplet correlations in Cooper pair splitters realized in a two-dimensional electron gas, *Nature Communications* **14**, 4876 (2023).
 - [11] G. Burkard, T. D. Ladd, A. Pan, J. M. Nichol, and J. R. Petta, Semiconductor spin qubits, *Rev. Mod. Phys.* **95**, 025003 (2023).
 - [12] G. Scappucci, C. Kloeffer, F. A. Zwanenburg, D. Loss, M. Myronov, J.-J. Zhang, S. De Franceschi, G. Katsaros, and M. Veldhorst, The germanium quantum information route, *Nature Reviews Materials* **6**, 926 (2021).
 - [13] J. T. Muhonen, J. P. Dehollain, A. Laucht, F. E. Hudson, R. Kalra, T. Sekiguchi, K. M. Itoh, D. N. Jamieson, J. C. McCallum, A. S. Dzurak, and A. Morello, Storing quantum information for 30 seconds in a nanoelectronic device, *Nature Nanotechnology* **9**, 986 (2014).
 - [14] M. Tao, S. Agarwal, D. Udeshi, N. Basit, E. Maldonado, and W. P. Kirk, Low Schottky barriers on n-type silicon (001), *Applied Physics Letters* **83**, 2593 (2003).
 - [15] A. Dimoulas, P. Tsipas, A. Sotiropoulos, and E. K. Evangelou, Fermi-level pinning and charge neutrality level in germanium, *Applied Physics Letters* **89**, 252110 (2006).
 - [16] T. Nishimura, K. Kita, and A. Toriumi, Evidence for strong Fermi-level pinning due to metal-induced gap states at metal/germanium interface, *Applied Physics Letters* **91**, 123123 (2007).
 - [17] K. Aggarwal, A. Hofmann, D. Jirovec, I. Prieto, A. Sammak, M. Botifoll, S. Marti-Sanchez, M. Veldhorst, J. Arbiol, G. Scappucci, J. Danon, and G. Katsaros, Enhancement of proximity-induced superconductivity in a planar ge hole gas, *Phys. Rev. Res.* **3**, L022005 (2021).
 - [18] F. Vigneau, R. Mizokuchi, D. C. Zanuz, X. Huang, S. Tan, R. Maurand, S. Frolov, A. Sammak, G. Scappucci, F. Lefloch, and S. De Franceschi, Germanium quantum-well josephson field-effect transistors and interferometers, *Nano Letters* **19**, 1023 (2019).
 - [19] N. W. Hendrickx, D. P. Franke, A. Sammak, M. Kouwenhoven, D. Sabbagh, L. Yeoh, R. Li, M. L. V. Tagliaferri, M. Virgilio, G. Capellini, G. Scappucci, and M. Veldhorst, Gate-controlled quantum dots and superconductivity in planar germanium, *Nature Communications* **9**, 2835 (2018).
 - [20] J. Ridderbos, M. Brauns, J. Shen, F. K. de Vries, A. Li, E. P. A. M. Bakkers, A. Brinkman, and F. A. Zwanenburg, Josephson effect in a few-hole quantum dot, *Advanced Materials* **30**, 1802257 (2018).
 - [21] A. Tosato, V. Levajac, J.-Y. Wang, C. J. Boor, F. Borsoi, M. Botifoll, C. N. Borja, S. Marti-Sanchez, J. Arbiol, A. Sammak, M. Veldhorst, and G. Scappucci, Hard superconducting gap in germanium, *Communications Materials* **4**, 23 (2023).
 - [22] M. Valentini, O. Sagi, and L. e. a. Baghumyan, Parity-conserving cooper-pair transport and ideal superconducting diode in planar germanium, *Nat Commun* **15**, 10.1038/s41467-023-44114-0 (2024).
 - [23] E. Zhuo, Z. Lyu, and X. S. et al., Hole-type superconducting gatemon qubit based on ge/si core/shell nanowires, *npj quantum information* **9**, 10.1038/s41534-023-00721-9 (2023).
 - [24] M. Hinderling, S. ten Kate, M. Coraiola, D. Haxell, M. Stiefel, M. Mergenthaler, S. Paredes, S. Bedell, D. Sabonis, and F. Nichele, Direct microwave spectroscopy of andreev bound states in planar ge josephson junctions, arXiv preprint [arXiv:2403.03800](https://arxiv.org/abs/2403.03800) (2024).
 - [25] K. Itoh, W. Hansen, E. Haller, J. Farmer, V. Ozhogin, A. Rudnev, and A. Tikhomirov, High purity isotopically enriched 70ge and 74ge single crystals: Isotope separation, growth, and properties, *Journal of Materials Research* **8**, 1341–1347 (1993).
 - [26] F. Vigneau, F. Fedele, A. Chatterjee, D. Reilly, F. Kuemmeth, M. F. Gonzalez-Zalba, E. Laird, and N. Ares, Probing quantum devices with radio-frequency reflectometry, *Applied Physics Reviews* **10**, 021305 (2023).
 - [27] F. Borsoi, N. W. Hendrickx, V. John, M. Meyer, S. Motz, F. van Riggelen, A. Sammak, S. L. de Snoo, G. Scappucci, and M. Veldhorst, Shared control of a 16 semiconductor quantum dot crossbar array, *Nature Nanotechnology* **19**, 21 (2024).
 - [28] N. W. Hendrickx, W. I. L. Lawrie, M. Russ, F. van Riggelen, S. L. de Snoo, R. N. Schouten, A. Sammak, G. Scappucci, and M. Veldhorst, A four-qubit germanium quantum processor, *Nature* **591**, 580 (2021).
 - [29] D. Jirovec, A. Hofmann, A. Ballabio, P. M. Mutter, G. Tavani, M. Botifoll, A. Crippa, J. Kukucka, O. Sagi, F. Martins, *et al.*, A singlet-triplet hole spin qubit in planar ge, *Nature Materials* **20**, 1106 (2021).
 - [30] M. Leijnse and K. Flensberg, Coupling spin qubits via superconductors, *Phys. Rev. Lett.* **111**, 060501 (2013).
 - [31] M. Spethmann, S. Bosco, A. Hofmann, J. Klinovaja, and D. Loss, High-fidelity two-qubit gates of hybrid superconducting-semiconducting singlet-triplet qubits, *Physical Review B* **109**, 085303 (2024).
 - [32] A. Gyenies, A. Di Paolo, J. Koch, A. Blais, A. A. Houck, and D. I. Schuster, Moving beyond the transmon: Noise-protected superconducting quantum circuits, *PRX Quantum* **2**, 030101 (2021).
 - [33] M. Kjaergaard, M. E. Schwartz, J. Braumüller, P. Krantz, J. I.-J. Wang, S. Gustavsson, and W. D. Oliver, Superconducting qubits: Current state of play, *Annual Review of Condensed Matter Physics* **11**, 369 (2020).
 - [34] G. Kirsanskas, M. Goldstein, K. Flensberg, L. I. Glazman, and J. Paaske, Yu-shiba-rusinov states in phase-biased superconductor–quantum dot–superconductor junctions, *Phys. Rev. B* **92**, 235422 (2015).

- [35] A. Jellinggaard, K. Grove-Rasmussen, M. H. Madsen, and J. Nygaard, Tuning yu-shiba-rusinov states in a quantum dot, *Phys. Rev. B* **94**, 064520 (2016).
- [36] A. Bargerbos, M. Pita-Vidal, R. Zitko, J. Avila, L. J. Splitthoff, L. Grunhaupt, J. J. Wesdorp, C. K. Andersen, Y. Liu, L. P. Kouwenhoven, R. Aguado, A. Kou, and B. van Heck, Singlet-doublet transitions of a quantum dot josephson junction detected in a transmon circuit, *PRX Quantum* **3**, 030311 (2022).
- [37] J. Bauer, A. Oguri, and A. C. Hewson, Spectral properties of locally correlated electrons in a bardeen-cooper-schrieffer superconductor, *Journal of Physics: Condensed Matter* **19**, 486211 (2007).
- [38] T. Meng, S. Florens, and P. Simon, Self-consistent description of andreev bound states in josephson quantum dot devices, *Physical Review B* **79**, 224521 (2009).
- [39] T. Meng, S. Florens, and P. Simon, Self-consistent description of andreev bound states in josephson quantum dot devices, *Phys. Rev. B* **79**, 224521 (2009).
- [40] W. I. L. Lawrie, H. G. J. Eenink, N. W. Hendrickx, J. M. Boter, L. Petit, S. V. Amitonov, M. Lodari, B. Paquelet Wuetz, C. Volk, S. G. J. Philips, G. Droulers, N. Kalhor, F. van Riggelen, D. Brousse, A. Sammak, L. M. K. Vandersypen, G. Scappucci, and M. Veldhorst, Quantum dot arrays in silicon and germanium, *Applied Physics Letters* **116**, 080501 (2020).
- [41] A. Sammak, D. Sabbagh, N. W. Hendrickx, M. Lodari, B. Paquelet Wuetz, A. Tosato, L. Yeoh, M. Bollani, M. Virgilio, M. A. Schubert, P. Zaumseil, G. Capellini, M. Veldhorst, and G. Scappucci, Shallow and undoped germanium quantum wells: A playground for spin and hybrid quantum technology, *Advanced Functional Materials* **29**, 1807613 (2019).
- [42] E. Lee, X. Jiang, and M. e. a. Houzet, Spin-resolved andreev levels and parity crossings in hybrid superconductor-semiconductor nanostructures, *Nature Nanotechnology* **9**, 79–84 (2014).
- [43] K. Grove-Rasmussen, H. I. Jorgensen, B. M. Andersen, J. Paaske, T. S. Jespersen, J. Nygaard, K. Flensberg, and P. E. Lindelof, Superconductivity-enhanced bias spectroscopy in carbon nanotube quantum dots, *Phys. Rev. B* **79**, 134518 (2009).
- [44] L. Yu, Bound states in paramagnetic impurity-containing superconductors, *Chinese Journal of Physics* **21**, 21 (1965).
- [45] H. Shiba, Classical Spins in Superconductors, *Progress of Theoretical Physics* **40**, 435 (1968).
- [46] A. I. Rusinov, Superconductivity near a Paramagnetic Impurity, *Letters to JETP* **9**, 146 (1969).
- [47] B. M. Andersen, K. Flensberg, V. Koerting, and J. Paaske, Nonequilibrium transport through a spinful quantum dot with superconducting leads, *Phys. Rev. Lett.* **107**, 256802 (2011).
- [48] V. V. Baran, E. J. Frost, and J. Paaske, Surrogate model solver for impurity-induced superconducting sub-gap states, *Physical Review B* **108**, L220506 (2023).
- [49] M. Tinkham, *Introduction to Superconductivity*, 2nd ed. (Dover Publications, 2004).
- [50] P. Fulde, High field superconductivity in thin films, *Advances in Physics* **22**, 667 (1973).
- [51] F. van Riggelen, N. W. Hendrickx, W. I. L. Lawrie, M. Russ, A. Sammak, G. Scappucci, and M. Veldhorst, A two-dimensional array of single-hole quantum dots, *Applied Physics Letters* **118**, 044002 (2021).
- [52] M. W. A. de Moor, J. D. S. Bommer, D. Xu, G. W. Winkler, A. E. Antipov, A. Bargerbos, G. Wang, N. van Loo, R. L. M. O. het Veld, S. Gazibegovic, D. Car, J. A. Logan, M. Pendharkar, J. S. Lee, E. P. A. M. Bakkers, C. J. Palmstrøm, R. M. Lutchyn, L. P. Kouwenhoven, and H. Zhang, Electric field tunable superconductor-semiconductor coupling in majorana nanowires, *New Journal of Physics* **20**, 103049 (2018).
- [53] A. E. Antipov, A. Bargerbos, G. W. Winkler, B. Bauer, E. Rossi, and R. M. Lutchyn, Effects of gate-induced electric fields on semiconductor majorana nanowires, *Phys. Rev. X* **8**, 031041 (2018).
- [54] N. Hendrickx, D. Franke, and A. e. a. Sammak, Fast two-qubit logic with holes in germanium, *Nature* , 487–491 (2020).
- [55] N. Hendrickx, D. Franke, and A. e. a. Sammak, A single-hole spin qubit, *Nature Communications* (2020).
- [56] N. W. Hendrickx, L. Massai, M. Mergenthaler, F. Schupp, S. Paredes, S. W. Bedell, G. Salis, and A. Fuhrer, Sweet-spot operation of a germanium hole spin qubit with highly anisotropic noise sensitivity (2023), [arXiv:2305.13150 \[cond-mat.mes-hall\]](https://arxiv.org/abs/2305.13150).
- [57] P. Chandra, P. Coleman, and R. Flint, Hysteric order in the heavy-fermion compound Uru_2Si_2 , *Nature* **493**, 621 (2013).
- [58] S. Bosco, M. Benito, C. Adelsberger, and D. Loss, Squeezed hole spin qubits in ge quantum dots with ultrafast gates at low power, *Phys. Rev. B* **104**, 115425 (2021).
- [59] K. Laubscher, J. D. Sau, and S. Das Sarma, Germanium-based hybrid semiconductor-superconductor topological quantum computing platforms: Disorder effects, *arXiv preprint arXiv:2404.16285* (2024).

METHODS

Fabrication

The device is fabricated on a Ge/SiGe heterostructure, which is grown on n-type Si(001) substrate using a reduced pressure chemical vapor deposition reactor. The stack comprises of a reverse graded $\text{Si}_{0.2}\text{Ge}_{0.8}$ virtual substrate, a 16 nm Ge quantum well, a 27 nm $\text{Si}_{0.2}\text{Ge}_{0.8}$ barrier, and a less than 1 nm Si sacrificial cap [41]. The device is fabricated in three electron-beam lithography defined layers separated by two oxide layers of ~ 7 nm Al_2O_3 grown by atomic layer deposition at 300°C . The first layer forms the PtGeSi contacts after lithography; a wet etch is performed using buffered HF ($\sim 6\%$) solution to remove the sacrificial cap before a 15 nm Pt layer is deposited via e-gun evaporation at a pressure of 1×10^{-7} mbar. The Pt contacts then undergo rapid thermal annealing at 400°C for 15 min in argon atmosphere. Barrier gates and plunger gates are deposited using e-gun evaporation and consist of a Ti (5 nm) sticking layer and a Pd layer (25 nm and 29 nm for the barrier and plunger layers respectively).

Measurement

The device is measured inside a sample puck loaded into a Bluefors XLD dilution refrigerator, at a mixing chamber temperature of ~ 9 mK. The dilution refrigerator is equipped with a (1-1-6) T vector magnet, the

sample chip being placed such that the 6 T direction is in-plane. We expect the main source of magnetic field misalignment to result from misalignment of the sample board inside the puck (QDevil QBoard sample holder) during sample loading. We estimate this error to be less than 5° . Differential conductance measurements are taken using a Stanford-Research Systems SR860 lock-in amplifier at a frequency of 119 Hz, and amplitude of $2.5 \mu\text{V}$. A line resistance of $2.7 \text{ k}\Omega$ is subtracted in all measurements. As we use a superconducting tunnel probe for our measurements, tunnelling events between the superconducting lead and the quantum dot manifest at an offset energy of $\Delta_0 = 72 \mu\text{eV}$. Bias spectroscopy measurements contain a small thermally induced bias offset of $18 \mu\text{eV}$, which has been subtracted from all relevant data. DC gate voltages are applied via a QDevil QDAC-II voltage source.

In addition to lock-in measurements, radiofrequency reflectometry was performed as described in the Supplementary Information, using a FPGA with a built in microwave signal generator as well as signal demodulator (Quantum Machines OPX+). A tank circuit with a resonance frequency of 192.3 MHz was used, connected to the drain contact. The incident rf-signal is attenuated by 40 dB at various plates of the cryostat, and undergoes an additional attenuation of 20 dB from a directional coupler at the MXC plate (See Supplementary Section Figure 2). The reflected signal undergoes 40 dB of amplification at the 4 K stage via a HEMT amplifier, and passes through a DC block and bias-tee at the input of the demodulation circuit. A 50Ω terminator is connected to the DC side of the bias-tee.

Supplementary Information: A proximitized quantum dot in germanium

Lazar Lakic^{†,1} William Iain L. Lawrie^{†,1} David van Driel,² Lucas E. A. Stehouwer,² Menno Veldhorst,² Giordano Scappucci,² Ferdinand Kuemmeth,¹ and Anasua Chatterjee^{1,2,*}

¹*Center for Quantum Devices, Niels Bohr Institute,
University of Copenhagen, 2100 Copenhagen, Denmark*

²*QuTech and Kavli Institute of Nanoscience, Delft University of Technology, Delft, The Netherlands*
(Dated: May 10, 2024)

In the Supplementary Information we present additional data as well as a minimal model for our hybrid system. In section I, we present data in a low regime of coupling between the superconductor (SC) and quantum dot (QD) that showcases the tunability of our system and complements the results presented in the main article. We also present similar results measured using radiofrequency (RF) reflectometry, a technique ubiquitous for spin-based qubits, crucial to develop readout for hybrid superconductor-semiconductor devices incorporating quantum dots, such as Kitaev chains. Section II describes critical field measurements for different orientations of the applied magnetic field. Finally, Section III presents a qualitative model of the observed spectrum of our proximitized quantum dot.

Section I. Low Γ_S B-field Studies in Transport and RF-Reflectometry

We study the magnetic field dependence of the subgap states in a regime of low coupling between SC and QD, complementary to the strong-coupling regime in the main text.

Setting the tunnel barriers to $V_{RB} = -1.3$ V and $V_{LB} = -0.83$ V, we tune the QD into a many-hole regime using the plunger gate PG. We perform bias spectroscopy at 0 mT, observing filling of the QD with eye-like features characteristic of YSR states as described in the main text, and shown in Figure S1a. In Figure S1b the out-of-plane magnetic field is set to 100 mT, revealing lifting of what we believe is sub-gap spin degeneracy of the $|D\rangle$ groundstate, as indicated by the black arrows.

In Figure S1c the splitting is increased as shown by the black arrows, when we apply a field of 200 mT. We then configure the PG to $V_{PG} = -2.236$ V at the sub-gap splitting in Figure S1c (orange notch), and vary the out-of-plane magnetic field as seen in Figure S1d. A Zeeman splitting is measured in bias spectroscopy starting from 0 mT. Extracting the g-factor using the standard Zeeman formula yields a $g_{\perp} = 4.5 \pm 0.6$, consistent with previous experimental findings of large g-factors in planar Ge/SiGe, and ~ 3 times larger than the g-factor we found for the strongly hybridized system described in the main text in this study. As the magnetic field is rotated along the principal axis at a perpendicular field of 200 mT a strong anisotropy is seen, in agreement with previous studies carried out in planar Ge/SiGe.

Remaining in a low-coupling regime ($V_{RB} = -1.3$ V, $V_{LB} = -0.83$ V), we proceed to tune the QD to a few-hole regime and perform bias spectroscopy using standard reflectometry methods[1] using a cryogenic tank circuit with a frequency of 192.3 MHz (Figure S2a). A typical RF excitation voltage at the sample is 3 μ V, which is applied and demodulated using a Quantum Machines OPX+. Figure S2 shows the normalized demodulated signal V_{RF} .

Figures S2c-e depict Coulomb diamonds measured at magnetic field strengths of 0 mT, 750 mT and 990 mT respectively, in the few-hole, lower-coupling regime described in this Supplementary Information section. Suppression of transport exists in an energy window of gap of $\pm 2\Delta$, as well as Coulomb diamonds with charging energies exceeding 2 mV. The x-axis is labeled with a virtual parameter δV_{PG} , where $\delta V_{PG} = 0$ corresponds to $V_{PG} = -1.8215$ sweeping 15 mV above and below. Figures S2c-e depict bias spectroscopy from which we extract g_{\perp} outside the superconducting gap. Figures S2f-h correspond to zoomed-in plots of figures S2c-e, revealing a magnetic field dependent splitting. The extracted g-factor is $g = 5.3 \pm 0.8$, in agreement within error with the sub-gap spin splitting that we measured using low-frequency transport techniques, in Figure S1.

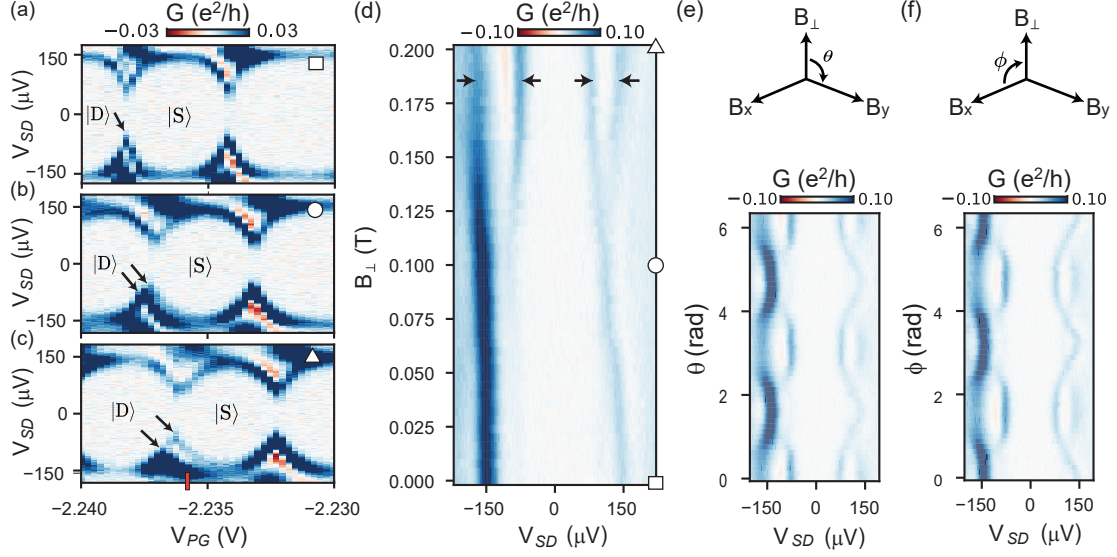


FIG. S1. **(a-c)** Bias spectroscopy with tunnel barriers set to $V_{RB} = -1.3$ V and $V_{LB} = -0.83$ V, at 0 mT (square in (a)), 100 mT (circle in (b)) and 200 mT (triangle in (c)). Black arrows indicate spin splitting at the transition between a $|D\rangle$ GS and a $|S\rangle$ GS. **(d)** Magnetic field sweep at $V_{PG} = -2.236$ V (orange notch in (c)), showing spin-splitting of the odd-occupied state. We extract an out of plane g -factor of $g_{\perp} = 4.5 \pm 0.6$. **(e-f)** Bias spectroscopy as a function of magnetic field angle at total magnetic field strength $|B| = 200$ mT and $V_{PG} = -2.236$ V. Above each panel, we state the rotational angle with respect to the sample direction. A strong g -tensor asymmetry is observed for the QD between out-of-plane and in-plane magnetic field orientations.

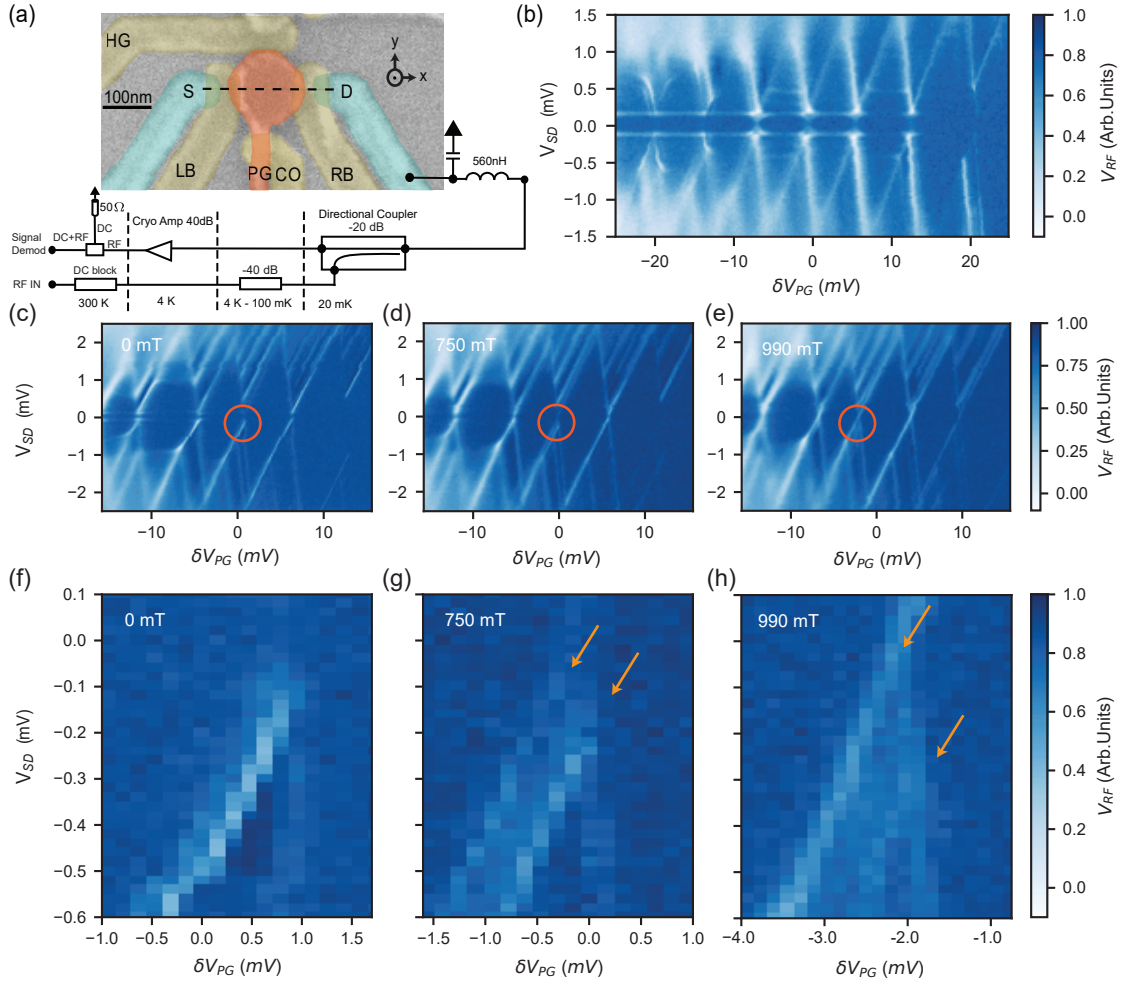


FIG. S2. **(a)** False coloured SEM of a nominally identical device, including the RF-reflectometry setup used to measure the data in the following panels. **(b)** Coulomb diamonds obtained at tunnel barrier values of $V_{RB} = -1.25$ V, $V_{LB} = -0.72$ V. **(c-e)** Bias spectroscopy, measured using RF reflectometry, at 0 mT (c), 750 mT (d) and 990 mT (e). **(g-h)** Zoomed-in scan within the region marked by orange circles in panels c-e respectively. Orange arrows indicate spin splitting, with a g -factor of $g = 5.3 \pm 0.8$.

Section II. Measurements of Critical Field

We perform bias spectroscopy as a function of magnetic field in Figure S3a-c, with the device configured in the few-hole regime. Figure S3b shows the critical in-plane field parallel to the direction of transport (see Figure S2a for a definition of the x direction). This configuration is expected to have a higher critical field than the perpendicular magnetic direction due to a smaller surface area, thus making it harder for the magnetic field flux to pin and destroy superconductivity. Finally, Figure S3c depicts the critical in-plane field perpendicular to the direction of transport (see Figure S2a for a definition of the y direction). The critical field in this direction is marginally lower than the out-of-plane magnetic field.

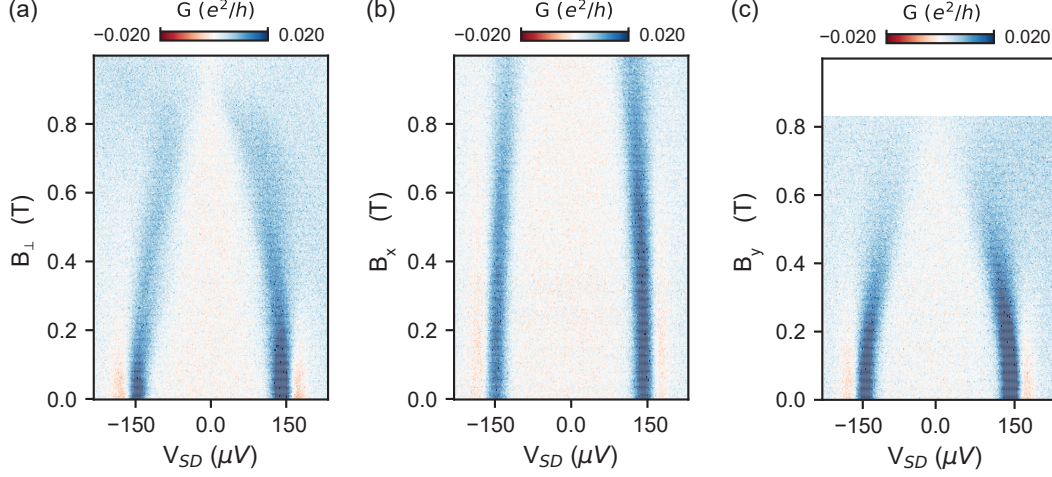


FIG. S3. (a) Magnetic field sweep from 0 to 1 T out of plane with respect to the device. (b) Magnetic field sweep from 0 to 1 T for in-plane field, parallel to the direction of transport (c) Magnetic field sweep from 0 to 0.82 T for in-plane field, perpendicular to the direction of transport.

Section III. Modeling of Subgap States

The device in the main text consists of a QD weakly coupled to one superconducting lead, and strongly coupled to another. We therefore write the Hamiltonian of the total system as:

$$H = H_{QD} + H_T + H_{SC}. \quad (1)$$

Where H_{QD} is defined as

$$H_{QD} = \sum_{\sigma} \epsilon d_{\sigma}^{\dagger} d_{\sigma} + U d_{\downarrow}^{\dagger} d_{\downarrow} d_{\uparrow}^{\dagger} d_{\uparrow} + \frac{E_z}{2} (d_{\uparrow}^{\dagger} d_{\uparrow} - d_{\downarrow}^{\dagger} d_{\downarrow}) \quad (2)$$

Here, ϵ is the electrochemical potential, U is the charging energy and E_z is the Zeeman energy. As one superconducting lead is weakly coupled, we consider only one bulk superconductor for H_{SC} , and ignore possible phase differences between their order parameters. In the superconducting Anderson impurity model, H_{SC} consists of a sum over multiple orbitals in the superconductor. Following Refs. [2, 3], we replace this sum by a single orbital and write:

$$H_{SC} = \xi \sum_{\sigma} c_{\sigma}^{\dagger} c_{\sigma} - \Delta (c_{\uparrow}^{\dagger} c_{\downarrow}^{\dagger} + h.c.) + \frac{E_z^{SC}}{2} (c_{\uparrow}^{\dagger} c_{\uparrow} - c_{\downarrow}^{\dagger} c_{\downarrow}) \quad (3)$$

Where ξ is the single-electron energy, Δ is the parent gap and E_z^{SC} is the Zeeman energy. We set $\xi = 0$, as the superconductor is grounded throughout the experiment. The Zeeman splitting of the superconductor is commonly excluded, as metallic superconductors usually have significantly lower g factors than the semiconductors they are coupled to. We however choose not to exclude it, in view of the low in-plane g-factor of Ge/SiGe heterostructure QDs, as well as the little-known magnetic field behavior of the novel PtGeSi superconductor. Finally, we can write the coupling of the superconductor and QD as:

$$H_T = \Gamma_S \sum_{\sigma} (c_{\sigma}^{\dagger} d_{\sigma} + h.c.) \quad (4)$$

where Γ_S is the spin-conserving hybridization energy. The full basis consists of 16 states, which we write as the tensor product of the number states of the superconductor and QD $|SC, QD\rangle$:

$$\{|0, 0\rangle, |\uparrow, 0\rangle, |\downarrow, 0\rangle, |2, 0\rangle, |0, \uparrow\rangle, |\uparrow, \uparrow\rangle, |\downarrow, \uparrow\rangle, |2, \uparrow\rangle, |2, \downarrow\rangle, |\uparrow, \downarrow\rangle, |\downarrow, \downarrow\rangle, |2, \downarrow\rangle, |0, 2\rangle, |\uparrow, 2\rangle, |\downarrow, 2\rangle, |2, 2\rangle\} \quad (5)$$

To model the spectrum, we consider excitations between the even and odd parity states. As the tunnel probe is a superconductor, we offset all excitation energies by Δ .

In Main Text Fig. 4b,c a Zeeman splitting of the superconductor was required to match the model to the experiment. For the model overlays seen in main text Figure 4a-c, the parameters used were a superconducting gap of $\Delta = 72 \mu\text{eV}$, a charging energy of $U = 1.6 \text{ meV}$, a hybridization energy of $\Gamma_S = 110 \mu\text{eV}$ along with an energy splitting on both SC and QD. We phenomenologically include the magnetic field dependence of the parent gap as: $\Delta(B) = 2\Delta_0 \sqrt{1 - (B/B_c)^2}$, where the factor of 2 is due to both leads having a superconducting density of states, resulting in quasiparticle transport between the bulk superconductors at $E = 2\Delta$ and $B_c = 0.9 \text{ T}$ as the critical field. This is required for agreement between the experimental data and the model, as states are observed at $E_{\text{state}} + \Delta$ due to the superconducting tunnel probe.

Using the described ZBW model we can compute the energy spectrum of the QD hybridizing with the SC. In S4d and g, we adding a Zeeman energy of $E_z = 56 \mu\text{eV}$ to the QD energy and nothing on the superconductor, which results in a spin-splitting at the charge degeneracy points $\epsilon(\Delta) = 0$ and $\epsilon(\Delta) = -1.6$, but no splitting in the even parity regions ($|S\rangle$), contradicting the data in Figure S4g. In supplement Figure S4e and h, we add a Zeeman energy of $E_z = 56 \mu\text{eV}$ only to the SC, resulting in a splitting in the even parity states ($|S\rangle$) resembling the energy separation seen in main text Figure 4b-c, however we see no spin-splitting at the charge degeneracy points $\epsilon(\Delta) = 0$ and $\epsilon(\Delta) = -1.6$; furthermore, the characteristic eye-like curvature of the $|D\rangle$ state is significantly reduced, and does not match the data in Figure S4h. In Figure S4f and i, a Zeeman energy $E_z = 56 \mu\text{eV}$ was added to both the QD and the SC, resulting in qualitative agreement to the data in Figure S4i. We stress that our model is quite simple and is not meant to fit the data quantitatively, and as such the magnitude and sign of the respective Zeeman terms have not been varied extensively. For example, future theoretical work could include the spin-orbit coupling, as well as a more detailed description of the superconductor beyond zero band width.

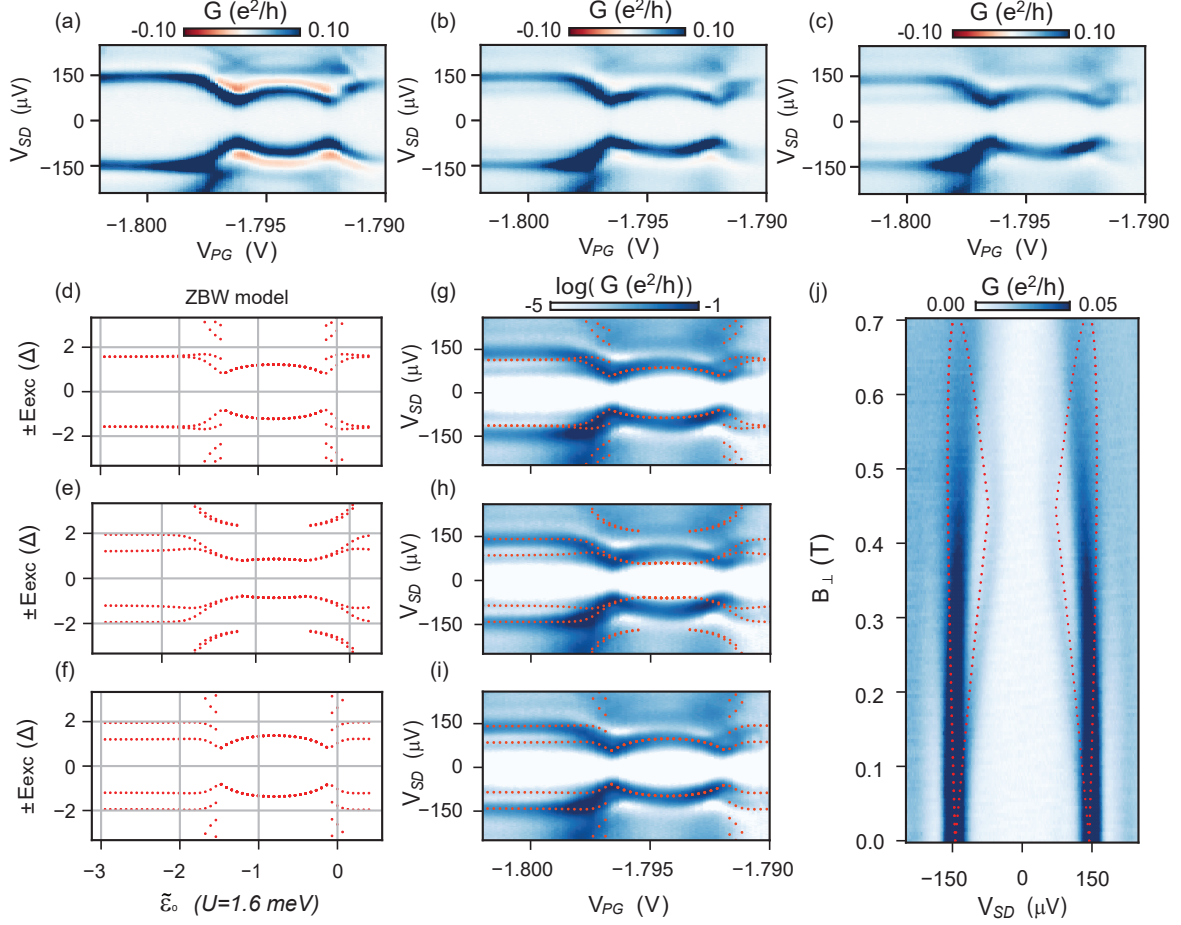


FIG. S4. **(a-c)** Bias spectroscopy data from main text Figures 4(a-c) without the logarithmic scale. **(d)** Excitation energy in units of $\Delta = 72\mu\text{eV}$ as a function of chemical potential in units of charging energy $U = 1.6$ meV, with a Zeeman energy only on the QD of $E_z=56$ μeV . **(e)** Excitation energy in units of $\Delta = 72\mu\text{eV}$ as a function of chemical potential in units of charging energy $U = 1.6$ meV, with a Zeeman energy of $E_z=56$ μeV on SC only. **(f)** Excitation energy in units of $\Delta = 72\mu\text{eV}$ as a function of chemical potential in units of charging energy $U = 1.6$ meV, Zeeman energy on both SC and QD of $E_z=56$ μeV . **(g-i)** Bias spectroscopy data from main Figure 4c, overlaid with the computed model (orange) from supplement Figure 4d-f respectively. **(j)** Bias spectroscopy data from main Figure 4d overlaid with the computed ZBW model (orange) correcting for the gap closing as the magnetic field increases using a g-factor of 1.5 on both SC and QD.

Finally, in Fig S4j we show the bias spectroscopy data from main text Figure 4d, overlaid with the computed ZBW spectrum. There is a good agreement between the model and the data until about 400 mT, when the splitting becomes larger than the SC pairing energy. We attribute this discrepancy between model and data to the ZBW model, which cannot model the Zeeman effect on a bulk superconducting density of states.

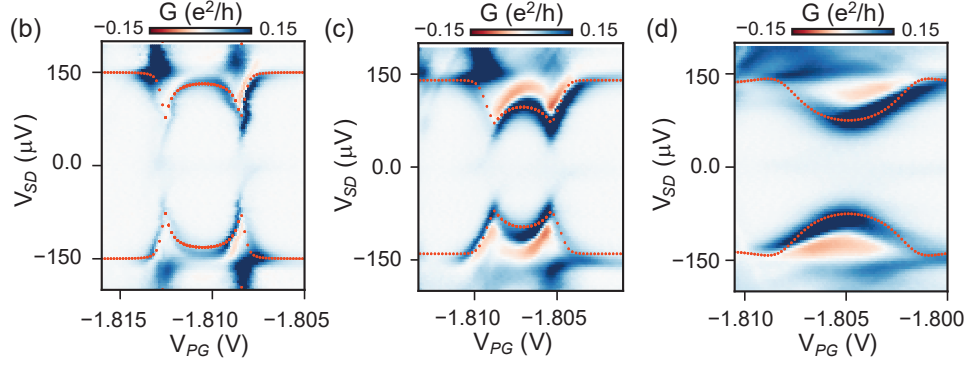


FIG. S5. **(a)** Bias spectroscopy data from main text Figure 2b overlaid with the computed ZBW model, setting the gap energy to $\Delta_0 = 75 \mu\text{eV}$, a charging energy of $U = 1.6 \text{ meV}$ and a $\Gamma_S = 70 \mu\text{eV}$ a) without the logarithmic scale. **(b)** Bias spectroscopy data from main text Figure 2c overlaid with the computed ZBW model, setting the gap energy to $\Delta_0 = 72 \mu\text{eV}$, a charging energy of $U = 1.6 \text{ meV}$ and a $\Gamma_S = 110 \mu\text{eV}$. **(c)** Bias spectroscopy data from main text Figure 2d overlaid with the computed ZBW model, setting the gap energy to $\Delta_0 = 66 \mu\text{eV}$, a charging energy of $U = 1.6 \text{ meV}$ and a $\Gamma_S = 150 \mu\text{eV}$.

Extracting Hybridization Energy

In order to quantify the the hybridization energy of SC and QD Γ_S , we model the sub-gap states in main text Figure 2b-d in the ZBW model, using the superconducting gap and charging energy extracted in the main text. We manually tune the parameter Γ_S until a qualitative match between data and model is found. For Fig S5a we set the SC gap to $\Delta_0 = 75 \mu\text{eV}$, the charging energy to $U = 1.6 \text{ meV}$, for which we extract an estimate of $\Gamma_S = 70 \mu\text{eV}$. In Fig S5b the SC gap is set $\Delta_0 = 72 \mu\text{eV}$, the charging energy to $U = 1.6 \text{ meV}$, yielding an estimate on the QD-SC of $\Gamma_S = 110 \mu\text{eV}$. Fig S5c is the fully coupled groundstate, in order to model this the SC gap is set to $66 \mu\text{eV}$, the charging energy to 1.6 meV estimating the SC-QD coupling to be $\Gamma_S = 150 \mu\text{eV}$

[†] These authors contributed equally.

* anasua.chatterjee@tudelft.nl

- [1] F. Vigneau, F. Fedele, A. Chatterjee, D. Reilly, F. Kuemmeth, M. F. Gonzalez-Zalba, E. Laird, and N. Ares, Probing quantum devices with radio-frequency reflectometry, *Applied Physics Reviews* **10**, 021305 (2023).
- [2] T. Meng, S. Florens, and P. Simon, Self-consistent description of andreev bound states in josephson quantum dot devices, *Physical Review B* **79**, 224521 (2009).
- [3] J. Bauer, A. Oguri, and A. Hewson, Spectral properties of locally correlated electrons in a bardeen-cooper-schrieffer superconductor, *Journal of Physics: Condensed Matter* **19**, 486211 (2007).